Moderate-aspect-ratio elliptical cylinders in simple shear with inertia

By C. M. ZETTNER AND M. YODA†

G. Woodruff School of Mechanical Engineering, Georgia Institute of Technology, Atlanta,
GA 30332–0405, USA

The effects of fluid inertia, geometry and flow confinement upon the dynamics of neutrally buoyant elliptical and non-elliptical cylinders over a wide range of aspect ratios in simple shear are studied experimentally for moderate shear-based Reynolds numbers Re. Unlike circular cylinders, elliptical cylinders of moderate aspect ratio cease to rotate, coming to rest at a nearly horizontal equilibrium orientation above a critical Reynolds number Re_{cr} ('stationary behaviour'). Simple dynamics arguments are proposed to explain the effects of aspect ratio and flow confinement upon critical Reynolds number and particle dynamics. Experiments confirm results from previous numerical simulations that the normalized rotation period for $Re < Re_{cr}$ ('periodic behaviour') is proportional to $(Re_{cr} - Re)^{-0.5}$ for small $Re_{cr} - Re$. For periodic behaviour, maximum and minimum angular cylinder speeds both decrease, and period increases, as $Re_{cr} - Re$ decreases. For stationary behaviour, the cylinder rotates until it achieves a nearly horizontal equilibrium orientation, which increases as the Reynolds number approaches the critical value. The experimental results are in good agreement with previous lattice-Boltzmann simulations for a 0.5 aspect ratio cylinder.

Variation in angular speed over a rotation period decreases as aspect ratio increases, while Re_{cr} increases as flow confinement and aspect ratio increase. A non-elliptical cylinder of 0.33 aspect ratio also ceases to rotate above a certain Reynolds number. Although Re_{cr} is different from the corresponding elliptical case, the scaling of the normalized rotation period for this body as $Re_{cr} \to Re$ is identical to that for the elliptical cylinder, suggesting that this scaling is independent of particle shape (i.e. 'universal', as conjectured in previous numerical studies). The results also demonstrate that a variety of centrosymmetric bodies with aspect ratios below unity transition from periodic to stationary behaviour.

1. Introduction

The study of bluff bodies immersed in a simple shear (linearly varying, zero-mean) flow is important in understanding the effects of particle geometry upon inertial, or non-zero Reynolds number, suspension flows. A basic two-dimensional model for a dilute neutrally buoyant inertial suspension is a freely rotating (torque-free) single neutrally buoyant circular cylinder suspended about a fixed central axis in shear at non-zero shear-based Reynolds number $Re \equiv a^2 G/v$. Here, a is the characteristic particle dimension (circular cylinder radius or largest half-dimension of an ellipsoid), G is the flow shear rate, and v the kinematic viscosity of the fluid.

† Author to whom correspondence should be addressed: minami.yoda@me.gatech.edu

In experiments, the flow is always confined by the test section walls. Moreover, current technology limits time-dependent simulations of this flow to relatively small computational domains. Flow confinement, characterized by the ratio of cylinder diameter to test section width $\kappa = 2a/L$, is hence an important issue in these sheared bluff-body flows. The stability limit for simple shear, or plane Couette, flow (Tillmark & Alfredsson 1992) imposes an upper limit upon the Reynolds number achievable in experiments of

$$Re \leqslant 350\kappa^2. \tag{1.1}$$

Note that (1.1) is an upper limit; simple shear flow disturbed by a bluff body is probably less stable than its undisturbed counterpart. Numerical results for flat plates (Barkley & Tuckerman 1999) and experimental results for circular cylinders (Bottin *et al.* 1998) show that even small bodies ($\kappa \leqslant 0.05$) destabilize plane Couette flow, significantly reducing the transition channel-based Reynolds number below its undisturbed value of roughly 350.

Kossack & Acrivos (1974) have shown that the flow around a circular cylinder in shear deviates from the Stokes flow solution for $Re > 1.0$, while Poe & Acrivos (1975) have shown that it deviates from the perturbation solution for $Re > 0.1$. In general, two streamlines crossing at two stagnation points divide the centrosymmetric, or antisymmetric, flow into five regions: two reversed flow regions to the 'left' and 'right' of the body; two continuing flow regions 'above' and 'below' the body; and a closed streamline region surrounding the freely rotating cylinder. Neither the inviscid nor the Stokes flow solutions predict this closed streamline region.

Although Poe & Acrivos (1975) reported that confinement had negligible effects for $\kappa < 0.32$, independent numerical (Ding & Aidun 2000) and experimental (Zettner & Yoda 2001) studies have shown that confinement has a marked effect upon this flow at higher κ. Flow confinement causes normalized rotation rate to decay more slowly with Reynolds number (roughly as $Re^{-0.3}$ for $\kappa = 0.39$, vs. $Re^{-0.5}$ for unconfined flow). Zettner & Yoda (2001) proposed a simple model to explain these flow confinement and inertial effects at moderate Re.

Although the steady two-dimensional dynamics of circular cylinders in simple shear are reasonably well understood over a large range of Reynolds numbers, little is known about the behaviour of other bluff bodies at non-zero Reynolds number. The elliptical cylinder in simple shear is a fundamental unsteady two-dimensional bluff-body flow. Moreover, it represents a first step towards understanding how particle geometry affects suspension dynamics, and ultimately extending models of suspensions of perfectly smooth spherical particles to actual three-dimensional suspensions with particles of varying roughness and shape. The experimental study of this flow is interesting in terms of understanding both sheared bluff-body flows and particle–fluid interactions in suspensions.

In comparison with circular and spherical bodies, there is little previous work on ellipses and ellipsoids in simple shear. Jeffery (1922) studied the motion of a neutrally buoyant solid ellipsoid described by the equation

$$\left(\frac{x'}{a}\right)^2 + \left(\frac{y'}{b}\right)^2 + \left(\frac{z'}{c}\right)^2 = 1, \tag{1.2}$$

where (x', y', z') are the three principal axes of the ellipsoid (and hence define a body-fixed coordinate system), and (a, b, c) are the dimensions of the ellipsoid along these axes, respectively, in an arbitrary unbounded Stokes flow, or $Re = 0$. Closed-form analytical solutions were derived for an unbounded simple shear with the velocity

field $u = Gy$ and where the z'-axis of the ellipsoid is fixed along the direction of vorticity. The coordinate system (x, y, z) defines the undisturbed shear flow with x along the flow direction, y along the velocity gradient direction, and z along the vorticity direction. The ellipsoid rotates around the z-axis at rate $\Omega(t) = \dot{\theta}(t)$ where t is time and θ is angular orientation. The angular orientation, velocity and period (θ, Ω and T, respectively) are then

$$\theta = \tan^{-1} \left\{ \frac{1}{AR} \tan \left[\frac{(AR)Gt}{1 + (AR)^2} \right] \right\}, \tag{1.3}$$

$$\frac{\Omega}{G} = \frac{\sin^2(\theta) + (AR)^2 \cos^2(\theta)}{1 + (AR)^2}, \tag{1.4}$$

$$TG = \frac{2\pi \left[1 + (AR)^2 \right]}{AR}, \tag{1.5}$$

where $AR = b/a \leqslant 1$ is the ellipsoid aspect ratio. Note that these Jeffery's orbit solutions are independent of c, the ellipsoid dimension along the axis of rotation. The numerical simulations by Aidun, Lu & Ding (1998) for elliptical cylinders in simple shear at $Re = 0.02$ have shown that (1.3)–(1.5) are also valid for the elliptical cylinder case, where $c \to \infty$, at $Re \approx 0$. Equation (1.4) implies that the maximum and minimum angular speeds will occur when the cylinder is vertical and horizontal, respectively.

Consider an elliptical cylinder fixed symmetrically in plane Couette flow of width L with speed U_b at the moving walls, giving a shear rate $G = 2U_b/L$ (figure 1a). The elliptical cross-section has semi-major axis a, semi-minor axis b, and aspect ratio $AR = b/a$ ($0 < AR \leqslant 1$), giving a shear-based Reynolds number $Re = a^2 G/\nu$. For the circular cylinder ($AR = 1$), the values for angular velocity and period reduce to the classic Stokes flow solutions, with $\Omega/G = 0.5$ and $GT = 4\pi$.

Feng & Joseph (1995) used quasi-steady and direct numerical simulations to investigate the relative contributions of particle and unsteady fluid inertia in the two-dimensional flow of a neutrally buoyant $AR = 0.5$ ellipse in simple shear at $Re = 0.25$ and $\kappa = 0.1$. They confirmed that the ellipse dynamics closely follow a Jeffery's orbit at $Re = 0.25$, with the inertial terms only slightly affecting the rotation.

Aidun *et al.* (1998) solved the time-dependent lattice-Boltzmann equation for the two- and three-dimensional flow around a neutrally buoyant ellipse and ellipsoid, respectively, freely and symmetrically suspended in simple shear. The flow transitioned from a time-periodic state to a stationary state above a critical Reynolds number $Re_{cr} \approx 7.25$ and 20 for the ellipse and ellipsoid, respectively. For $Re < Re_{cr}$, Aidun *et al.* reported that $GT \propto (Re_{cr} - Re)^{-0.5}$ as $Re_{cr} - Re \to 0$.

Ding & Aidun (2000, referred to in the rest of this paper as DA00) extended these simulations to an ellipse and oblate spheroid, both at $AR = 0.5$ and $\kappa = 0.2$, for particle-to-fluid density ratios ρ_p/ρ_f ranging from 0.25 to 100. They observed the same type of transition as Aidun *et al.* (1998), and showed that the transition was through a saddle–node bifurcation. DA00 concluded from their results that

$$GT \propto |p - p_{cr}|^{-0.5} \quad \text{for} \quad |p - p_{cr}| \to 0, \tag{1.6}$$

where p is some dimensionless flow parameter such as Re or ρ_p/ρ_f and p_{cr} is the value of this parameter at the transition. Based on the form of the transition (i.e. saddle–node bifurcation), they further hypothesized that this scaling was 'universal', or independent of particle shape, flow confinement and density ratio.
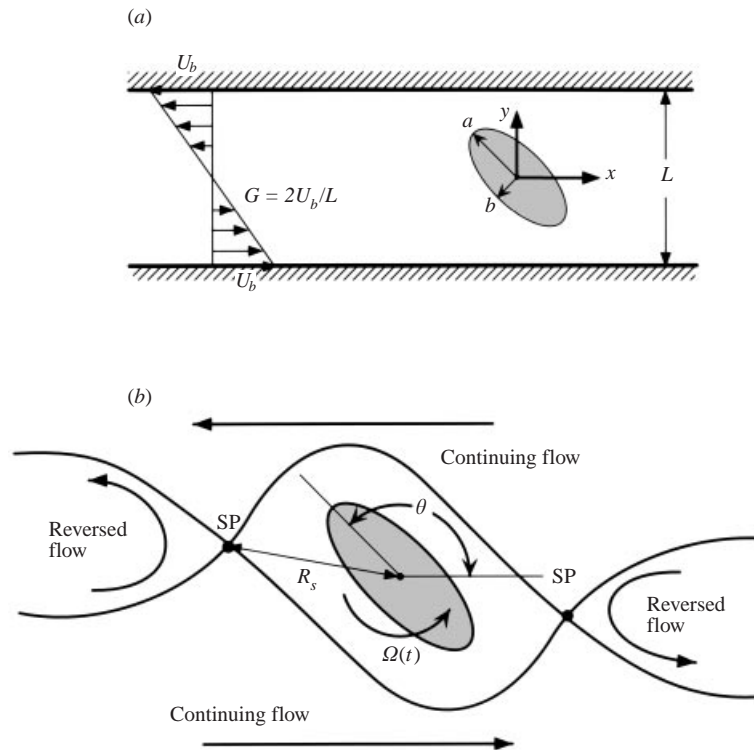
(a)

(b)

FIGURE 1. (a) Definition sketch for a $2a \times 2b$ elliptical cylinder in confined simple shear in a channel of width L with maximum speed U_b. (b) Schematic of the flow around the cylinder showing the two off-surface stagnation points (SP), the continuing flow regions, and the reversed flow regions. θ is the angular position of the cylinder from the horizontal, $\Omega(t)$ is its angular speed, and R_s is the distance from the cylinder centre to either stagnation point.

In the time-periodic state, the flow streamlines were similar to those for the circular cylinder case, with streamlines crossing at two off-surface stagnation points (indicated by SP on figure 1b) and dividing the flow into two reversed flow regions, two continuing flow regions, and a central region that rotates with the body (figure 1b). Unlike the circular cylinder, this central flow region is not closed and the streamlines contact the rotating cylinder for a portion of the rotation. In the stationary state, the body comes to a complete rest at a nearly horizontal angular orientation θ_o. DA00 found that the minimum torque on a fixed ellipse of any orientation is positive for $Re \leqslant Re_{cr}$. For $Re > Re_{cr}$, however, the net torque is negative when the body orientation exceeds θ_o but is less than π, indicating that θ_o is a stable equilibrium orientation.

This behaviour is unexpected, given that the actual rotation rate Ω of a circular cylinder in simple shear increases and Ω/G decreases, implying that $\Omega/G \to 0$ for large Re. Given these surprising numerical results for elliptical cylinders at moderate Re for $AR = 0.5$ and 1.0, experiments were carried out for a wide range of neutrally buoyant elliptical cylinders to study how AR and κ affect particle and fluid dynamics. A single non-elliptical cylinder was also studied to examine if the scaling of DA00 was 'universal'. To our knowledge, this work is the first experimental investigation of this flow, and the first to address flow confinement and certain particle geometry issues. The experimental facility and data analysis are detailed in the following section. Section 3 describes the results for $4 \leqslant Re \leqslant 25$ for elliptical cylinders of $0.22 \leqslant AR \leqslant 1$
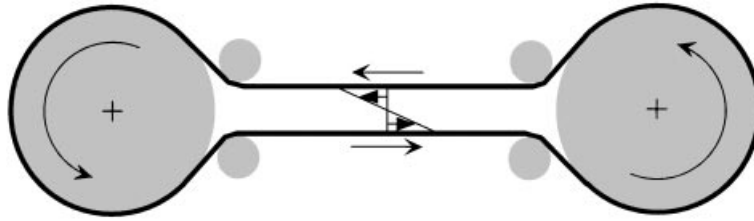
FIGURE 2. Top view of the plane Couette flow facility, showing the endless belt, large rollers, and small rollers.

at confinement ratios $0.31 \leqslant \kappa \leqslant 0.5$. The results are analysed and discussed in §4, and the simple model previously proposed for circular cylinders is extended to explain the observed geometric effects.

2. Experimental setup and data analysis

The experimental facility and data analysis procedures used to investigate geometric effects (described by AR) and confinement effects (characterized by κ) upon the cylinder and flow dynamics for the elliptical cylinder in simple shear are described in this section. Elliptical cylinders with $AR = 0.22$–1.0 and $\rho_p/\rho_f = 1$ in simple shear were studied for shear-based Reynolds numbers from 4 to 25 and $\kappa = 0.31$–0.5.

The plane Couette flow apparatus used in these experiments (figure 2) to create simple shear flow over a test section of width (extent along y, the velocity gradient direction) $L = 3.8$ cm and length (streamwise or x dimension) 35.6 cm is described in detail in Zettner & Yoda (2001). Based upon the design of Bech *et al.* (1995), simple shear flow is created inside a single, endless, tranparent belt supported by two parallel glass plates along the sides of the test section and driven by two large rollers at the ends of the test section. Two pairs of small rollers contract the test section to minimize end effects.

Steadiness, linearity and two-dimensionality of the flow in the test section were verified by measuring laser-Doppler velocimetry (LDV) velocity profiles in the (empty) test section for channel-based Reynolds numbers $Re_{ch} = U_b L/v = 120$–900 where U_b is the belt speed. Velocity profile linearity and two-dimensionality are quantified by the mean deviation between the measured and expected x-component of the velocity (U and U_e, respectively) normalized by U_b for each profile: $\varepsilon_1 \equiv \langle U - U_e \rangle / U_b$. Figure 3 shows U/U_b (vertical axis) as a function of channel position $2y/L$ (horizontal axis) for three different Re_{ch} and elevations (z-coordinate) in the test section. For $Re_{ch} < 275$ which corresponds to $Re < 22$ for $\kappa = 0.4$, $\varepsilon_1 < 5\%$ over a volume of the test section spanning -15.2 cm $\leqslant x \leqslant 15.2$ cm and -27.4 cm $\leqslant z \leqslant -3.8$ cm. Flow steadiness is quantified by the root-mean-square of the x-component of the velocity, u_{rms}, normalized by U_b: $\varepsilon_2 \equiv u_{rms}/U_b$. For $Re_{ch} < 400$ ($Re < 22$ for $\kappa = 0.33$), $\varepsilon_2 < 8.7 \times 10^{-3}$. Limiting Re_{ch} to 240 or Re to 19 for $\kappa = 0.4$ keeps $\varepsilon_1 < 5\%$ and $\varepsilon_2 < 4.1 \times 10^{-3}$ over about 80% of the axial length of the cylinders used for these experiments. Limitations upon steady rotation of the motor driving the facility restrict the minimum shear rate G in the facility to about $2.0 \, \mathrm{s}^{-1}$, corresponding to a minimum $Re = 4$ for $\kappa = 0.33$.

Elliptical cylinders were fabricated from three different materials for these experiments (dimensions and AR given in table 1): Pyrex (borosilicate glass) and epoxy resin cylinders for flow-field measurements and dynamics studies, and brass cylinders for dynamics studies. The two Pyrex cylinders were drawn hollow tubes fabricated by

Case	a (cm)	AR	κ	Material
Cylinder A	0.78	0.22	0.41	Epoxy resin
Cylinder B	0.62	0.27	0.33	Epoxy resin
Cylinder C	0.63	0.33	0.33	Pyrex (non-elliptical)
Cylinder D	0.62	0.33	0.33	Epoxy resin
Cylinder E	0.79	0.33	0.41	Epoxy resin
Cylinder F	0.63	0.50	0.33	Pyrex
Cylinder G	0.79	0.52	0.42	Epoxy resin
Cylinder H	0.60	0.69	0.32	Brass
Cylinder I	0.58	0.75	0.31	Brass
Cylinder J	0.75	1.0	0.39	Fused quartz
Cylinder K	0.95	1.0	0.50	Fused quartz

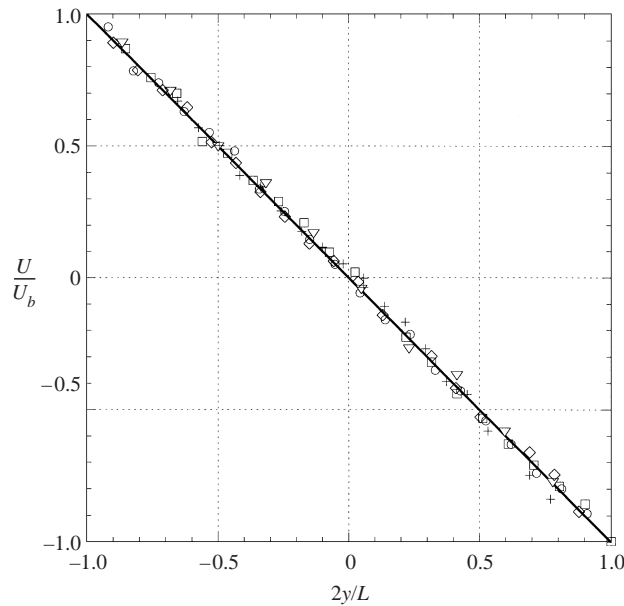TABLE 1. Cylinder dimensions and material.

FIGURE 3. Mean velocity profiles in empty Couette flow test section at $z = -6.4$ cm and Re_{ch}: 275 (circles), 209 (squares) and 125 (triangles); and also at $Re_{ch} = 275$, $z = -26.7$ cm (diamonds) and -15.3 cm (crosses). The solid line indicates ideal simple shear. The error is about the vertical extent of the symbols.

Precision Electronic Glass (Vineland, NJ). Both brass cylinders were constructed from 0.405 cm diameter brass tubing uniformly compressed along one axis to achieve the desired AR. The Pyrex and brass tubes were sealed at both ends with circular Pyrex end caps (diameter 1.27 cm and thickness 0.16 cm) with 0.038 cm diameter centred through-holes. The solid epoxy resin (DuPont Somos 7100) cylinders were built by the Rapid Prototyping and Manufacturing Institute, Georgia Institute of Technology (Atlanta, GA) with 0.15 cm or 0.20 cm diameter centred through-holes. The results from the elliptical cylinders are compared with those for fused quartz circular cylinders ($AR = 1$) from a previous investigation in the same facility (Zettner & Yoda 2001); the geometric characteristics of these cylinders are therefore also given in table 1.

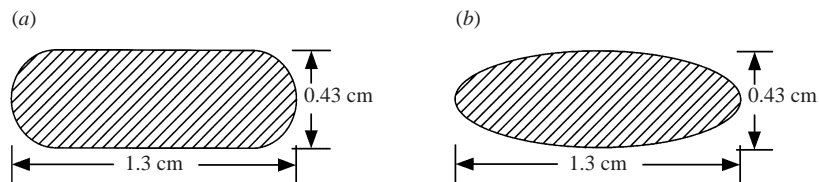All the cylinders had an axial length of 25.4 cm, or 26–41 times the maximum

(*a*) (*b*)

FIGURE 4. Sketches of an x, y cross-section of (*a*) non-elliptical Cylinder C $(AR, \kappa) = (0.33, 0.33)$ and (*b*) elliptical Cylinder D with the same (AR, κ).

cross-section dimension. End effects should be minor for these cylinders, based upon particle-image velocimetry data at different axial locations for the circular cylinder cases.

It was impossible to produce perfectly elliptical cylinders in all cases, given the various fabrication methods. The effects of deviation from elliptical cross-section were studied using two cylinders (Pyrex and epoxy resin) with the same $AR = 0.33$ and $\kappa = 0.33$ but different cross-sections. The epoxy cylinder was elliptical (within rapid prototyping tolerances of ± 0.1 mm), while the Pyrex cylinder was essentially a rectangle with rounded corners (figure 4).

The cylinders were suspended in the centre of the test section on a single 0.025 cm diameter monofilament passing through either the cylinder or the end cap through-holes, allowing the cylinders to freely rotate about their centres. The cylinders are therefore free to rotate but unable to translate. In all cases, the monofilament line was observed to remain straight and vertical during the experiments, confirming that the cylinder experienced no net force due to the flow. Given that a freely suspended particle symmetrically positioned in simple shear flow should experience no net force, the results of these experiments on particles should be directly comparable with the numerical simulations of DA00 on freely suspended particles.

All cylinders were density-matched to the surrounding fluid (i.e. neutrally buoyant). The brass, Pyrex, and fused quartz cylinders were partially filled with fluid to make them neutrally buoyant. Stainless steel capillary tubing (15 and 18 gauge or 0.18 and 0.13 cm outer diameter, respectively) was inserted into the central through-hole of the epoxy resin cylinders to make them neutrally buoyant; the monofilament then passed through the capillary tubing.

Three different working fluids are used in these experiments. An index- and density-matched aqueous solution of approximately 40% (w/w) glycerin and 36% (w/w) sodium iodide (index of refraction $n = 1.48$; density $\rho = 1.5\,\mathrm{g\,cm^{-3}}$; kinematic viscosity $v = 15$–20 cSt) is used with the transparent Pyrex cylinders. A density-matched aqueous solution of about 70% (w/w) glycerin with $v = 15$–20 cSt and $\rho = 1.25\,\mathrm{g\,cm^{-3}}$ is used with the opaque brass and epoxy resin cylinders. Finally, a third density-matched high-viscosity aqueous solution with $v = 30$–40 cSt and 75–77% (w/w) glycerin is used with Cylinder F $((AR, \kappa) = (0.50, 0.33))$ to carry out experiments at low Re.

Cylinder dynamics were studied by filming the cylinder at 30 Hz and 33 ms exposure time with a B/W CCD camera (TI Multicam CCD MC-1134P) and S-VHS VCR (Panasonic AG 1980P) on videotape. A mark on the top of the cylinder gave an absolute angular reference. Rotation period T was measured with a stopwatch during the recording; T was defined in these experiments to be the average rotation period over five full consecutive cylinder rotations. The maximum variation in the measured period was approximately 1% for periods up to 20 s and 3% for periods exceeding 60 s, corresponding to standard deviations of 0.02% and 0.04%, respectively.

Every tenth image (sampling rate = 3 Hz) was digitized from the videotape recording using a framegrabber card (ImageNation PX500) onto a 200 MHz PC HD. The cylinder angular position θ was determined with a MATLAB program from these images to within ± 0.02 radians. Angular velocity Ω was calculated from the θ data using a second-order central difference method; angular acceleration α was then calculated from Ω in the same fashion. To determine θ at the maximum and minimum angular velocities Ω_{max} and Ω_{min}, respectively, Ω was plotted as a function of θ over 2–4 cylinder revolutions, and a fourth-order polynomial was curve-fit to the data.

The elliptical cylinder was considered 'at rest' if it remained stationary for a minimum of 300 s, compared to the maximum rotation period observed in these experiments of about 120 s. The critical Reynolds number Re_{cr} was then defined as the maximum Re where there was rotation; in all cases save one, these values are within 0.3 of the minimum Re where the cylinder was at rest. For $AR = 0.33$ and $\kappa = 0.33$, Re_{cr} was within 1 of the minimum 'at rest' Re value. The greater uncertainty in this particular case was due to the extremely low Re_{cr} value, which was just above the minimum attainable Re in the experimental facility. In all cases, the Re_{cr} values were observed to be quite sensitive to any density mismatch between the cylinder and working fluid.

The flow-field dynamics were investigated using flow visualization and digital particle image velocimetry (PIV) (detailed in Zettner & Yoda 2001). The fluid is seeded with neutrally buoyant silver-coated hollow glass spheres with a mean diameter of 12.8 µm and a density of 1.3 g cm^{-3} (Potters Industries SH400S20) at a volume fraction of 5–10 p.p.m. An (x, y)-plane of the flow is illuminated with a 0.1 cm thick laser light sheet at a depth $z = -6.4$ cm below the free surface, near the centre of the cylinder. The width (x-extent) of the imaged flow region ranged in these experiments from 1.8 cm to 12 cm, corresponding to an image magnification of 0.07–0.358. The CCD camera used in the dynamics experiments images the motion of the tracer particles using frame straddling (Raffel, Willert & Kompenhans 1998), with an exposure time per frame of 3 ms and an interframe spacing within each pair of frames of 6–16 ms. The CCD frames are directly written via the framegrabber card to the 33 MB RAM of a 200 MHz PC as 480 row by 640 column 8-bit bitmap images.

The particle images were used to obtain both pathline and velocity information. Composite digital pathline images were obtained by superimposing up to 60 images, averaging grey scales and manually adjusting contrast and brightness. Velocity data were obtained from the particle images using a MATLAB cross-correlation-based PIV program with 32 pixel × 32 pixel interrogation windows and 50% overlap between adjacent windows. This window dimension corresponds to a spatial resolution of 0.73 mm at a magnification of 0.358 and 1.3 mm at a magnification of 0.07. Nearly instantaneous stagnation point locations were determined by bilinear interpolation of the PIV data.

3. Results

Rotation period T and angular position θ were measured over time t for elliptical cylinders with $AR = 0.22$–1.0, $\kappa = 0.31$–0.5 and $Re = 4$–25. For the range of Re studied, elliptical cylinders with moderate aspect ratios ($0.33 \leqslant AR \leqslant 0.52$) showed two distinct flow behaviours. For Re below a critical value Re_{cr}, the cylinder rotated with a constant period but time-varying angular speed (defined here as 'periodic behaviour'). For $Re > Re_{cr}$ ('stationary behaviour'), the cylinder remained at rest at a specific angular orientation θ_o. If the cylinder was released from an initial angular

Symbol	Case	AR	κ	Re_{cr}
cross	Cylinder A	0.22	0.41	Not observed (< 4)
plus	Cylinder B	0.27	0.33	Not observed (< 4)
filled diamond	Cylinder C	0.33	0.33	7.3 (non-elliptical)
no symbol	Cylinder D	0.33	0.33	4–5
square	Cylinder E	0.33	0.41	6
filled circle	Cylinder F	0.50	0.33	7.3
solid line or filled triangle	DA00	0.50	0.2	7.25
circle	Cylinder G	0.52	0.42	13.0
filled triangle	Cylinder H	0.69	0.32	Not observed (> 25)
filled inverted triangle	Cylinder I	0.75	0.31	Not observed (> 25)

TABLE 2. Critical Reynolds number Re_{cr} (when observed) for all elliptical cylinder cases studied. The various cylinders are identified by both a symbol and a letter.

orientation $\theta \neq \theta_o$, the cylinder rotated until $\theta = \theta_o$, remaining stationary at this orientation. For $Re = 4$–25, only periodic behaviour was observed for high-aspect-ratio (nearly circular) cylinders ($0.69 \leqslant AR \leqslant 1$), while only stationary behaviour was observed for low-aspect-ratio cylinders ($0.22 \leqslant AR \leqslant 0.27$). Periodic and stationary behaviours are discussed in detail in §§ 3.2 and 3.3.

In all pathline images and PIV vector plots shown, flow goes from right to left at the top and left to right at the bottom of the image. Only the right-hand half of the centrosymmetric flow is shown in all cases (i.e. the cylinder is on the left-hand side). Spatial coordinates, when given, are normalized by a; the centre of the cylinder is at the origin.

3.1. *Critical Reynolds number*

Table 2 gives the critical Reynolds numbers Re_{cr} (when observed) for all the elliptical cylinders. Increases in AR increase Re_{cr}, or delay transition to stationary behaviour. For an $AR = 0.33$ elliptical cylinder at $\kappa = 0.33$ (Cylinder D), $Re_{cr} = 4$–5. Increasing AR to 0.5 (Cylinder F) increases Re_{cr} to 7.3. The experimentally measured Re_{cr} for Cylinder F is in excellent agreement with the value of 7.25 obtained by DA00 in their lattice-Boltzmann simulations, despite the discrepancy in κ (0.2 for DA00, vs. 0.33 for Cylinder F). Confinement ratios below 0.33 appear therefore to have little effect upon Re_{cr}, similar to the circular cylinder case, where wall or confinement effects were observed to be negligible for $\kappa < 0.32$ (Poe & Acrivos 1975). Increases in κ above 0.32, however, do appear to increase Re_{cr}; increasing κ to 0.42 (Cylinder G) increases Re_{cr} to 13.0, vs. a Re_{cr} of 7.3 at $\kappa = 0.33$.

3.2. *Periodic behaviour* $(Re_{cr} - Re) > 0$

For periodic behaviour, T is a function of Re, κ and AR, reducing to Jeffery's solution (1.5) at $Re = 0$. Period non-dimensionalized by shear rate GT is plotted as a function of Re in figure 5 for $Re < Re_{cr}$ at $0.33 \leqslant AR \leqslant 0.52$ and all Re for $0.69 \leqslant AR \leqslant 1$. Data are presented for $0.33 \leqslant AR \leqslant 1.0$ and $0.2 \leqslant \kappa \leqslant 0.5$. The intermediate AR cases – $0.33 \leqslant AR \leqslant 0.52$ – show a large increase in GT just below their Re_{cr}. These results verify the numerical results of DA00 at $(AR, \kappa) = (0.5, 0.2)$ (solid line), who reported that $GT \to \infty$ as $Re \to Re_{cr}$. Moreover, the non-elliptical cylinder (filled diamond) case also shows this large increase in GT. In contrast, the high-aspect-ratio cylinders – $0.69 \leqslant AR \leqslant 1$ – show only a slight increase in GT over the entire range of Re observed. Given the trends observed for the other cases, this suggests that the
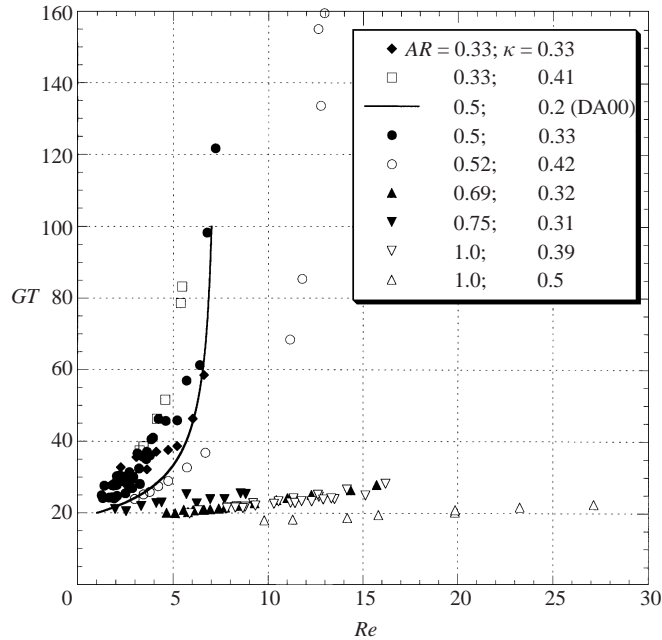
FIGURE 5. Plot of dimensionless period GT vs. shear-based Reynolds number Re for cylinders of $0.33 \leqslant AR \leqslant 1.0$ and $0.2 \leqslant \kappa \leqslant 0.5$. The various (AR, κ) cases and their corresponding symbols are given in the figure legend. Note that all cylinders are elliptical except for the $(AR, \kappa) = (0.33, 0.33)$ case (filled diamond). The maximum standard deviation in T is 0.04%. These experimental data are compared with the numerical results of DA00 (solid line).

critical Reynolds number of these high-AR cylinders (if it exists) lies well above the maximum observed Re.

The marked scatter in the $AR = 0.5$, $\kappa = 0.33$ (filled circles) data is mainly due to the use of several different viscosity (and composition) solutions to extend the minimum attainable Re. We also expect that the data at low Re have increased error since friction in the cylinder setup is comparable to viscous forces at these low G. Nevertheless, the experimental (filled circles) and numerical (solid line) data at $AR = 0.5$ are in good agreement for Reynolds numbers just below Re_{cr} even at different values of κ (0.33 vs. 0.2). This agreement between the experimental data and the two-dimensional numerical simulations confirms that end effects in the experiments due to the finite cylinder axial length of 25.4 cm are minimal.

The consistently higher experimental results are most likely due to friction in the cylinder mount (higher $T \Rightarrow$ lower Ω). Figure 6 compares normalized angular position θ/π of an $AR = 0.5$ elliptical cylinder as a function of non-dimensionalized time Gt for the numerical simulations of DA00 at $Re_{cr} - Re = 3.5$, $\kappa = 0.2$ (dashed line) and our experimental data at a similar $Re_{cr} - Re = 3.7$, $\kappa = 0.33$ (solid line). The effect of friction in the experiments is evident: by $Gt = 70$ (after about two full rotations), the experimental measurement lags the numerical result by half a rotation.

Figure 7 shows the non-dimensionalized rotation period GT vs. the difference between the critical and actual Reynolds numbers $Re_{cr} - Re$ on a log-log plot using the same symbols as in figure 5. As $Re_{cr} - Re \rightarrow 0$, DA00 showed that $GT \sim (Re_{cr} - Re)^{-0.5}$ for elliptical cylinders and ellipsoids, and conjectured that this scaling was independent of particle shape. All the elliptical cylinder cases where Re_{cr}
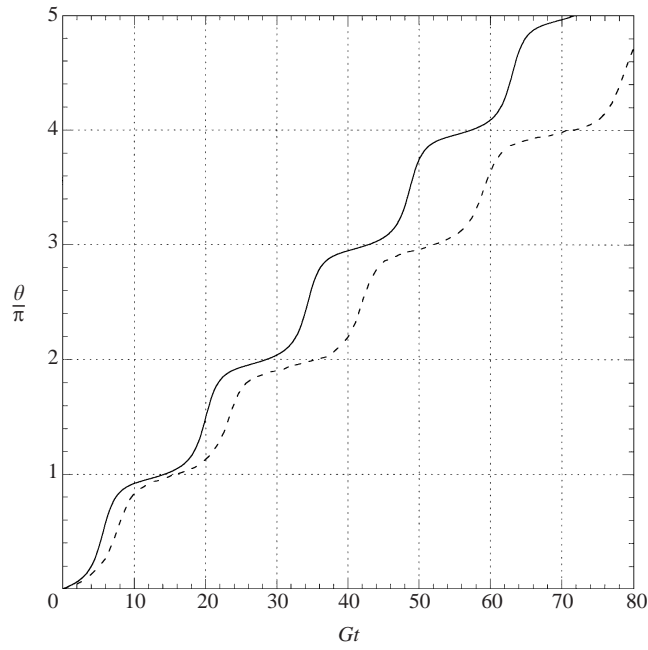
FIGURE 6. Normalized angular position θ/π vs. dimensionless time Gt for experimental data (dashed line) at $Re_{cr} - Re = 3.7$ at $\kappa = 0.33$ and numerical data (solid line) at $Re_{cr} - Re = 3.5$ at $\kappa = 0.2$, both for an $AR = 0.5$ elliptical cylinder. The error in the experimentally measured θ/π values is 0.006.
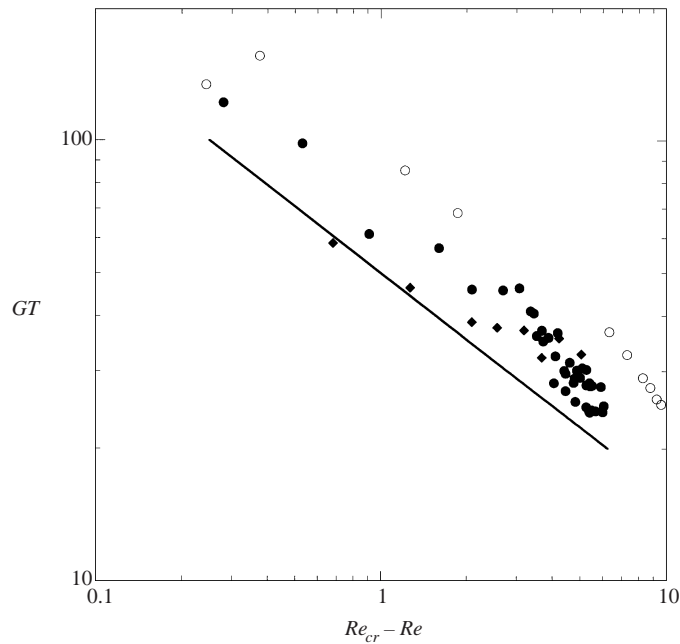

FIGURE 7. Log-log plot of dimensionless period GT as a function of the difference between the actual and critical Reynolds numbers $Re_{cr} - Re$. The symbols are identical to those used in figure 5.
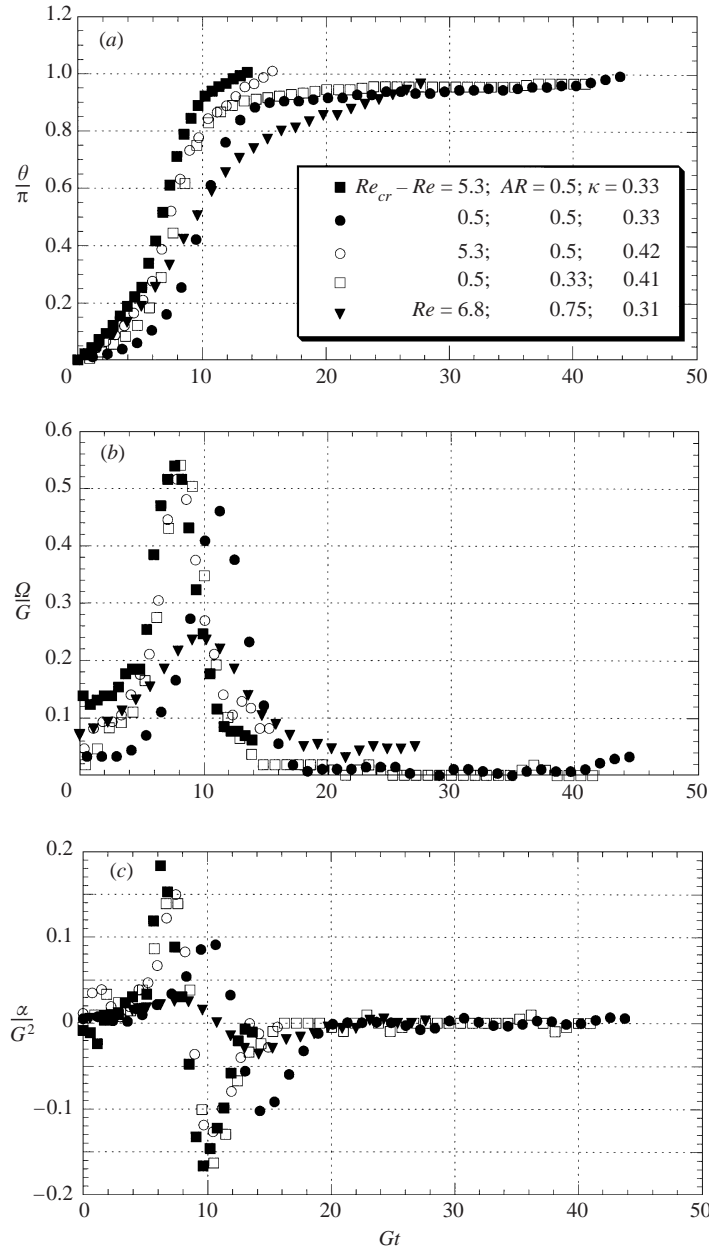
FIGURE 8. Normalized angular position θ/π (*a*), angular speed Ω/G (*b*) and acceleration α/G^2 (*c*) vs. normalized time Gt over half a revolution for five different elliptical cylinder cases. $Re - Re_{cr}$ or Re, AR and κ values for each case, along with the appropriate symbol, are given in the legend in (*a*). The error in the experimentally measured θ/π values is ± 0.006.

is observed in these experiments over a wide range of κ and AR follow the scaling relationship of DA00 for small $Re_{cr} - Re$. Moreover, this scaling also appears to hold for the nearly rectangular (non-elliptical) Cylinder C (filled diamond). Although this non-elliptical cylinder has a quite different Re_{cr} value from the corresponding elliptical case (Cylinder D), these data are in excellent agreement with the numerical

Cylinder (AR, κ)	$Re_{cr} - Re$ or Re	θ/π at Ω_{max} $(0.0 \leqslant \theta/\pi \leqslant 1.0)$	θ/π at Ω_{min} $(0.0 \leqslant \theta/\pi \leqslant 1.0)$
Jeffery's orbit (1.4)	$Re = 0$	0.50	1.00
Cylinder F (0.50, 0.33)	0.5	0.48	0.97
Cylinder F (0.50, 0.33)	5.3	0.54	0.95
Cylinder G (0.52, 0.42)	5.3	0.50	1.00
Cylinder I (0.75, 0.31)	$Re = 6.8$	0.51	0.96
Cylinder E (0.33, 0.41)	0.5	0.48	0.96
Cylinder C (0.33, 0.33) non-elliptical	5.1	0.48	1.00

TABLE 3. Angular position at maximum and minimum angular speed at various $Re_{cr} - Re$ or Re (if no Re_{cr} observed).

results of DA00 (solid line) for $Re_{cr} - Re < 1$, which has the same Re_{cr} but a different shape and AR.

Figure 8 shows the normalized angular orientation θ/π (*a*), speed Ω/G (*b*) and acceleration α/G^2 (*c*), which is proportional to the net torque, vs. dimensionless time Gt over a half-period for five cases which include four different cylinders, two differential Reynolds numbers ($Re_{cr} - Re$), two values of confinement and three aspect ratios. The figure includes a high-aspect-ratio case that exhibits only periodic behaviour (i.e. $Re_{cr} > 25$) at $(AR, \kappa) = (0.75, 0.31)$ and $Re = 6.8$ (filled inverted triangles). All the cylinders are at $\theta/\pi = 0$ at $t = 0$ and near $\theta/\pi = 1$ at the end of the half-period $t = 0.5T$. The area under each α/G^2 curve in figure 8(*c*) is zero, since the net torque is zero over a half-revolution. Measurements of angular orientation, speed and acceleration obtained every 0.33 s are shown over a half-period for each case. Note that the horizontal range and number of measurements (directly proportional to actual time) vary with each case due to variations in T.

The cylinder always rotates counterclockwise (i.e. $\Omega \geqslant 0$). Starting at $\theta = 0$ at $t = 0$ and minimum $\Omega/G > 0$, the cylinder accelerates to its maximum speed, passing rapidly through a vertical orientation ($\theta/\pi \approx 0.5$), then decelerates to a minimum velocity at a nearly horizontal position ($\theta/\pi \approx 1$). The error in the θ/π measurements is about 0.006. The normalized angular speed averaged over a full rotation is always significantly less than that for a circular cylinder at the same Re and κ (Zettner & Yoda 2001). In all cases, the maximum angular speed Ω_{max}/G (corresponding to zero α) is less than unity, and occurs at $Gt \approx 10$. As $Re_{cr} - Re$ decreases (i.e. $Re \rightarrow Re_{cr}$), both the non-dimensionalized angular speed and acceleration curves develop progressively longer 'tails', remaining nearly constant at a minimum value for long intervals (compare filled squares and circles with filled circles and squares for $Re_{cr} - Re = 5.3$ and 0.5). Since T increases sharply as $Re \rightarrow Re_{cr}$ (cf. figure 5), both cylinders at $Re_{cr} - Re = 0.5$ (filled circles, squares) remain nearly horizontal for almost half of an 18 s half-period. For fixed AR and κ, both Ω_{max}/G and Ω_{min}/G decrease as $Re_{cr} - Re$ decreases (filled squares and filled circles), in agreement with
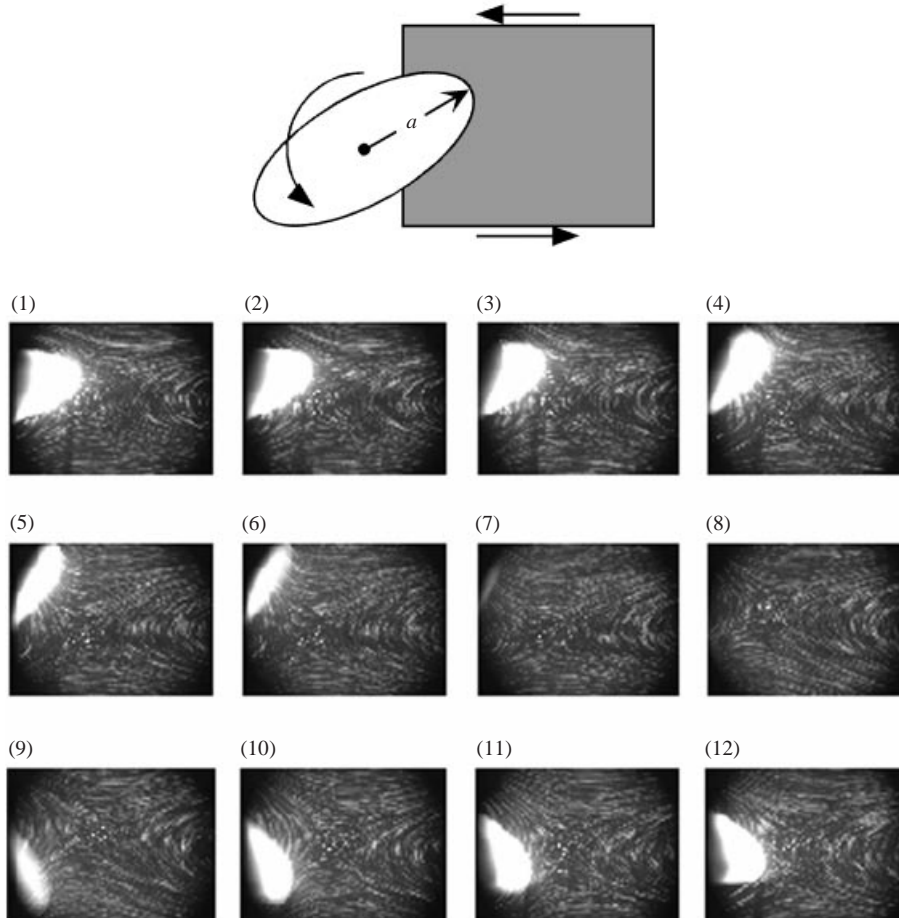
FIGURE 9. Sequential composite pathline images, each spanning 0.67 s and numbered in order, of elliptical Cylinder E $(AR, \kappa) = (0.33, 0.41)$ at $Re_{cr} - Re = 1.8$. The grey region in the definition sketch above the images shows the region visualized with respect to the ellipse, which is rotating counterclockwise.

the results of DA00 (cf. their figure 8). Although not shown here, θ, Ω, and α for non-elliptical Cylinder C show the same qualitative behaviour as $Re \to Re_{cr}$.

Cylinders at fixed AR and $Re_{cr} - Re$ with different Re and somewhat different κ (filled squares and circles for $\kappa = 0.33$ and 0.4, respectively) exhibit qualitatively similar dynamics, as predicted by (1.6). Flow confinement, at least over the range of κ studied, does not appear to have much effect upon cylinder dynamics at fixed AR and $Re_{cr} - Re$. Confinement does affect Re_{cr} for $\kappa > 0.33$; increasing confinement at a fixed AR and Re therefore increases $Re_{cr} - Re$, implying that both Ω_{max}/G and Ω_{min}/G increase. Comparison of filled circles and circles from figure 8(b) at the same Re of 6.7 but different $(Re_{cr} - Re)$, $AR = 0.5$, and $\kappa = 0.33$ and 0.42, respectively, shows this effect on Ω_{max}/G. Increasing AR decreases Ω_{max}/G and increases Ω_{min}/G (compare filled inverted triangles, filled circles with squares for $AR = 0.75$, 0.5 and 0.33), corresponding to a greatly reduced angular acceleration. Note that $\Omega_{min} \to \Omega_{max}$ and $\alpha \to 0$ for a circular cylinder $(AR = 1.0)$.

Table 3 lists the θ/π values at Ω_{max} and Ω_{min} for the cases shown in figure 6, Jeffery's solution, and non-elliptical Cylinder C. The maximum angular speed occurs when the
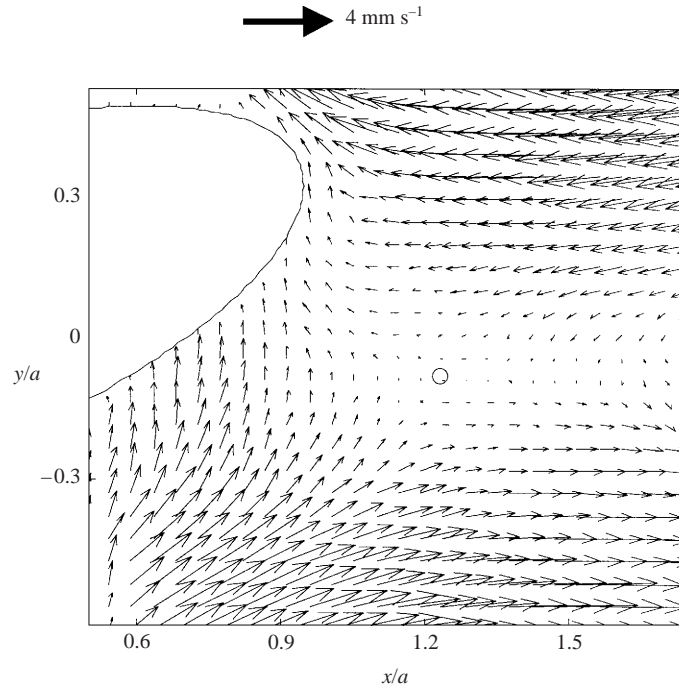
$\longrightarrow$ 4 mm s^{-1}

FIGURE 10. Close-up PIV vector plot of the flow around Cylinder E at $Re_{cr} - Re = 1.8$. This roughly corresponds to image 4 in figure 9.

ellipse is nearly vertical ($\theta/\pi \approx 0.5$) and the minimum speed occurs when the ellipse is essentially horizontal ($\theta/\pi \approx 1$). Moreover, these results appear to be independent of $Re_{cr} - Re$: Ω_{max} results obtained from over twenty Cylinder F cases exhibiting periodic behaviour at $0.3 \leqslant Re_{cr} - Re \leqslant 5.9$ gave $\theta/\pi = 0.47$–0.54. Similarly, the Ω_{max} results from eight non-elliptical Cylinder C cases for $0.7 \leqslant Re_{cr} - Re \leqslant 5.1$ gave Ω_{max} values ranging from 0.48 to 0.50. The larger variation in the θ/π values at Ω_{max} is due to our relatively poor angular resolution when sampling these high rotation rates at 30 Hz; the typical difference in consecutive angle measurements near Ω_{max} is $\Delta\theta/\pi = 0.06$, vs. $\Delta\theta/\pi = 0.005$ near Ω_{min}.

Figure 9 shows twelve sequential composite pathline images numbered in order, each spanning 0.67 s (20 frames), of an elliptical cylinder in simple shear rotating counterclockwise (along the shear direction) at $Re_{cr} - Re = 1.8$, $AR = 0.33$ and $\kappa = 0.41$ (Cylinder E). All the images are acquired at the same location in the flow. The cylinder, which is partially visible on the left-hand side of all images except 7 and 8, has maximum Ω in images 6 and 9 (note blurred edge), and minimum Ω in images 1 and 12. In all images, a reversed flow region is visible on the right, the two continuing flow regions are visible at the top and bottom, and a stagnation point is visible in the middle. The central streamline region, visible in images 7 and 8, is obscured by the cylinder in most of the images. Note the pathlines normal to the cylinder surface in images 5 and 6.

Stagnation point position varies significantly over these pathline images. PIV data were used to determine the location of the single stagnation point in this half of the antisymmetric flow. Figure 10 shows a representative PIV vector plot of the nearly instantaneous in-plane flow velocity components around an $AR = 0.33$ elliptical
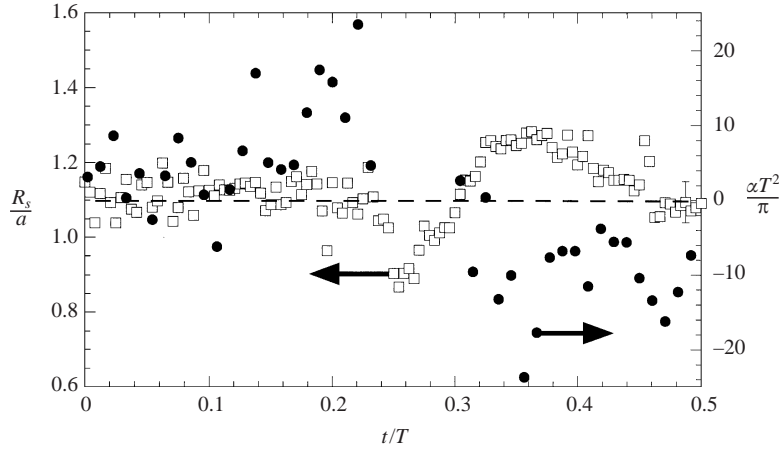
FIGURE 11. Normalized stagnation point distance R_s/a (open squares; left-hand scale) and acceleration α/G^2 (filled circles; right-hand scale) vs. dimensionless time t/T over half a rotation period for the flow shown in figure 9. The error bar represents two PIV grid cells.

cylinder at $Re_{cr} - Re = 1.8$ and $\kappa = 0.41$ (Cylinder E) at an angular position similar to image 4 in figure 9. The location of the off-surface instantaneous stagnation point at $(x/a, y/a) = (1.2, -0.1)$, corresponding to a radial distance from the cylinder centre $R_s/a = 1.2$, is indicated by a circle.

Figure 11 shows the normalized distance between the cylinder centre and the stagnation point R_s/a determined using PIV data (open squares; left-hand vertical scale) and angular acceleration α/G^2 (filled circles; right-hand scale), both vs. t/T for half a revolution of Cylinder E $(AR, \kappa) = (0.33, 0.41)$ at $Re_{cr} - Re = 1.8$. Time is defined so that at $t/T = 0$, the cylinder is at the angular orientation of image 1 in figure 9. Each datapoint for R_s/a is the stagnation point location averaged over 66 ms. $R_s/a = 1$ corresponds to the path traversed by the edge of the ellipse; R_s/a averaged over a full rotation is 1.1 at this Re. The error bar on the far right-hand side indicates the size of two PIV grid cells ($0.19a$ or 1.5 mm); we expect the experimental error to exceed the spatial resolution since R_s is determined from interpolated PIV data. The cylinder is not visible in the region imaged for $0.24 \leqslant t/T \leqslant 0.3$ (corresponding to images 7 and 8 in figure 9), so no speed and acceleration data were obtained over this interval. The α curve is nevertheless qualitatively similar to that in figure 8.

The stagnation point moves in towards the cylinder centre as the cylinder accelerates, with R_s/a reaching its minimum value of about 0.9 at $\alpha \approx 0$ (or at Ω_{max}). It then moves out from the centre as the cylinder decelerates, reaching a maximum R_s/a value of approximately 1.3 at minimum α (cf. figure 11). Although not shown here, PIV results at various Re show that the distance from the cylinder centre to the stagnation points averaged over a full rotation decreases as Re increases for a given (AR, κ), in agreement with observations for the $AR = 1$ circular cylinder (Zettner & Yoda 2001; DA00)

Periodic behaviour was also observed for high-aspect-ratio ($0.69 \leqslant AR \leqslant 1.0$) elliptical cylinders (Cylinders H, I, J and K). Although these cases followed the same trends as the intermediate AR cases for T, Ω and α as Re increased, they did not reach a critical Reynolds number and transition to stationary behaviour within the range of experimentally accessible $Re = 4$–25. We expect that a Re_{cr} does exist for
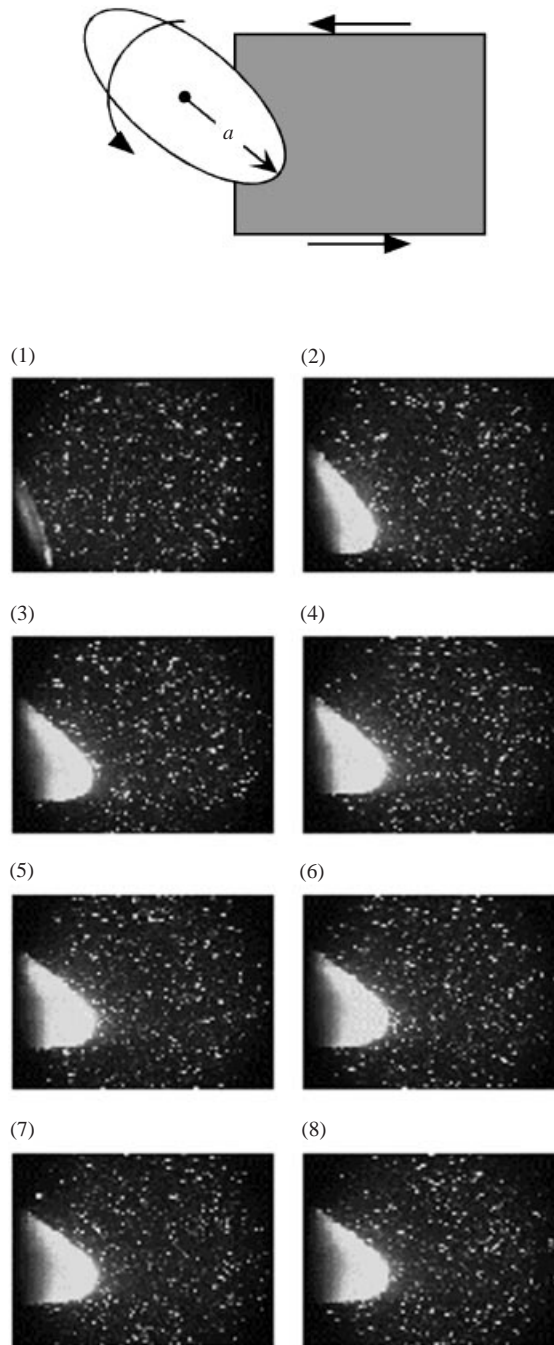
(1)   (2)

(3)   (4)

(5)   (6)

(7)   (8)

FIGURE 12. Sequential snapshots (33 ms exposure) numbered in order of Cylinder E at $Re_{cr} - Re = -2.0$ starting from rest. The cylinder accelerates and comes to rest at an equilibrium angle $\theta_o \approx \pi$ in the last image (8).

at least some of these high-AR cylinders, but this Re_{cr} value exceeds the maximum Reynolds number accessible with our facility. As AR approaches 1.0, however, the limitations upon the stability of the undisturbed simple shear (plane Couette) flow (cf. (1.1)) may also preclude the existence of a critical Reynolds number.
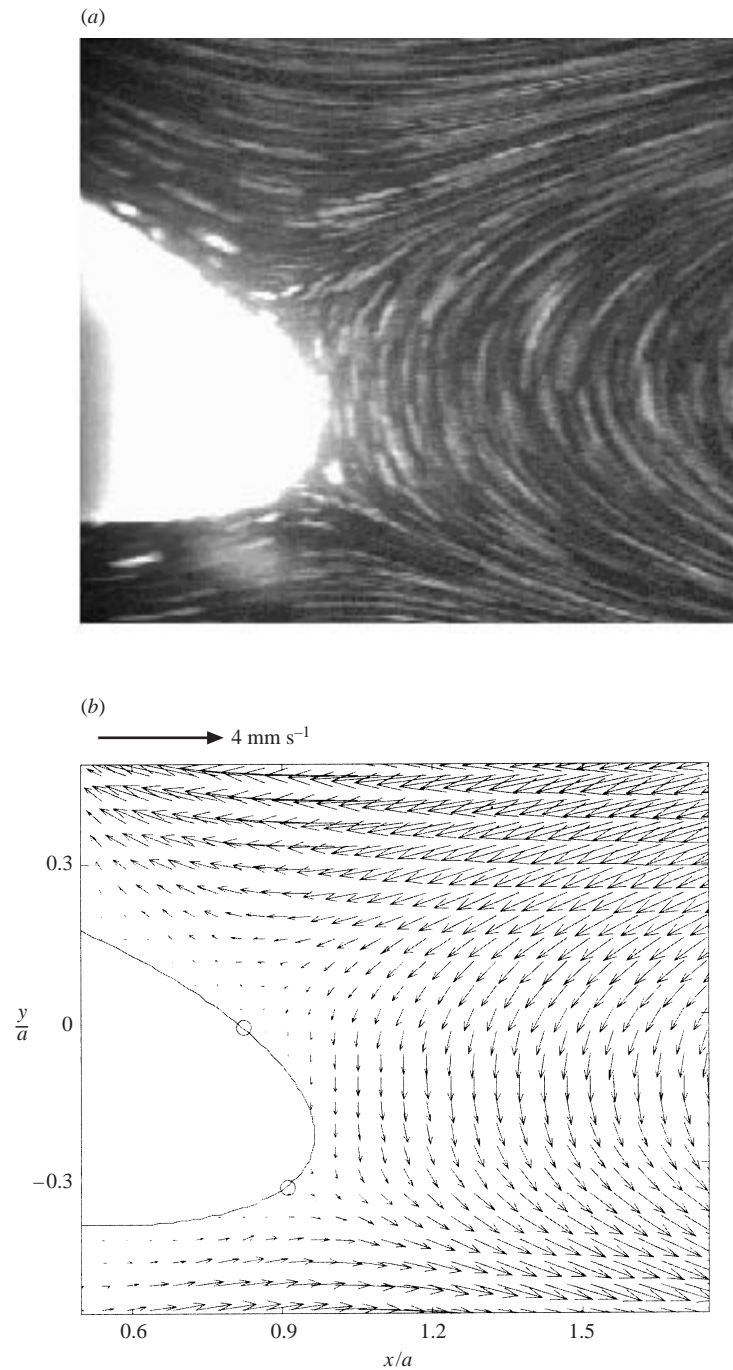
(*a*)

(*b*)

FIGURE 13. (*a*) Composite pathline image of Cylinder E at $Re_{cr} - Re = -2.0$ spanning 2 s; this image is composed of the 60 snapshots immediately following those of figure 12. The steadiness of the pathlines and the crisp cylinder boundary show that the cylinder remains at rest over this interval. (*b*) The corresponding PIV vector plot under identical conditions.
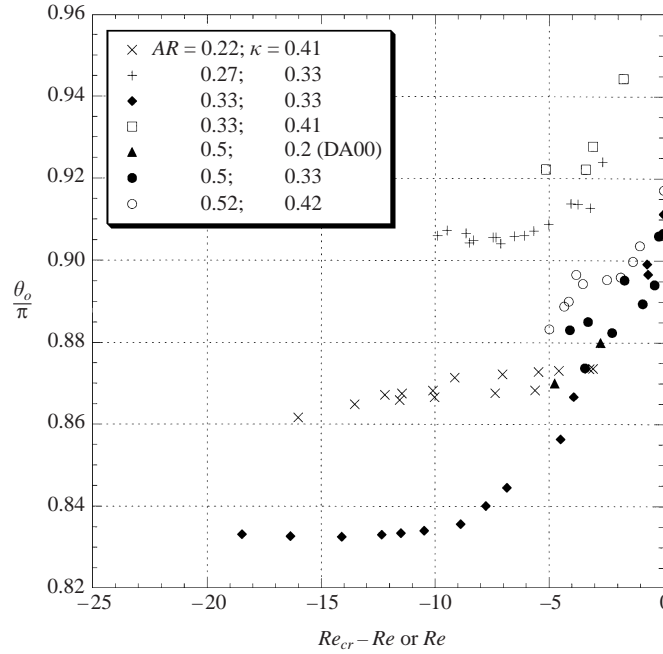
FIGURE 14. Plot of equilibrium angle θ_o/π vs. $Re_{cr} - Re$ or $-Re$ (if no Re_{cr} observed) for cylinders of $0.22 \leqslant AR \leqslant 0.52$ and $0.2 \leqslant \kappa \leqslant 0.42$. The various (AR, κ) values and their corresponding symbols are given in the figure legend. All cylinders are elliptical with the exception of the $(AR, \kappa) = (0.33, 0.33)$ case (filled diamonds). The results are compared with the numerical data of DA00 at $(AR, \kappa) = (0.50, 0.2)$ (filled triangles).

3.3. *Stationary behaviour* $(Re_{cr} - Re) < 0$

Figure 12 shows eight sequential instantaneous images (exposure $= 33$ ms) numbered in order and spaced 1 s apart for an $AR = 0.33$ elliptical cylinder starting from rest at $Re_{cr} - Re = -2$ and $\kappa = 0.41$ (Cylinder E). The cylinder accelerates and rotates counterclockwise, coming to rest at a nearly horizontal equilibrium orientation θ_o in the final image. The next 2 s (60 frames) of this sequence comprise the composite pathline image in figure 13(*a*). The pathlines (streamlines for this steady flow) are in good qualitative agreement with an instantaneous PIV vector plot of the flow around an $AR = 0.33$ cylinder at equilibrium for $Re_{cr} - Re = -2$ and $\kappa = 0.41$ (figure 13*b*). The two stagnation points on the cylinder surface in this half of the centrosymmetric flow are indicated by circles.

In all cases exhibiting stationary behaviour ($Re > Re_{cr}$ for $0.33 \leqslant AR \leqslant 0.69$ cylinders and all Re observed for $0.22 \leqslant AR \leqslant 0.27$ cylinders), the cylinder rotates from any initial orientation to a nearly horizontal orientation (i.e. θ_o is slightly less than π); θ_o does vary slightly, however, with Re, AR and κ. In contrast with periodic behaviour, the cylinder rotates clockwise (i.e. negative Ω, α and net torque) at a fixed $Re > Re_{cr}$ until it reaches the equilibrium orientation if released from rest at an initial orientation angle $\theta_o < \theta < \pi$. The cylinder rotates counterclockwise (i.e. positive Ω, α and net torque) when released from rest at $\pi < \theta < 2\pi + \theta_o$, clearly indicating that θ_o is a stable equilibrium angle. These results are in agreement with the numerical results of DA00.

Figure 14 shows the measured θ_o values normalized by π as a function of $Re_{cr} - Re$ for elliptical cylinders of $0.33 \leqslant AR \leqslant 0.52$ and $0.2 \leqslant \kappa \leqslant 0.42$ and a non-elliptical

cylinder of $AR = 0.33$ and $\kappa = 0.33$ (filled diamonds). θ_o/π results are also presented vs. $-Re$ for elliptical cylinders at $(AR, \kappa) = (0.22, 0.4)$ (crosses) and $(0.27, 0.33)$ (pluses); no Re_{cr} was observed for either cylinder, implying that Re_{cr}, if it exists, is less than 4. The experimental results are compared to the numerical results of DA00 for $AR = 0.33$, $\kappa = 0.2$ (filled triangles). The error in the θ_o/π measurements is approximately ± 0.006. As $Re_{cr} \to Re$, the equilibrium angle increases (i.e. the cylinder becomes more horizontal). The $AR = 0.5$ (filled circles) are in good agreement with the numerical results (filled triangles). Comparison of the results at different AR and κ implies that the equilibrium angle decreases as AR decreases, but increases as κ increases.

Cylinders with $AR = 0.22$ and 0.27 and $\kappa = 0.41$ and 0.33, respectively (Cylinder A and Cylinder B), exhibited only stationary behaviour within the range of Re studied. Jeffery's solution (1.5) predicts that these low-aspect-ratio cylinders will exhibit periodic behaviour as $Re \to 0$ with constant period $GT = 30$ and 25 for $AR = 0.22$ and 0.27, respectively. Limitations of the experimental facility precluded studies at Re below 4, so this behaviour could not be verified.

4. Discussion of results

Simple arguments are proposed in this section to explain the effects of AR and Re upon $\Omega(t)$ and AR and κ upon Re_{cr} observed and described in the previous section. The effects of geometry and their implications for actual non-colloidal particles are also briefly discussed.

4.1. *Angular speed $\Omega(t)$: periodic behaviour*

At large $Re_{cr} - Re > 0$, the elliptical cylinder rotates with time-varying angular speed. As $Re_{cr} - Re$ decreases (Re increases), the results from the previous section show that the maximum and minimum angular speeds both decrease for the cylinder. A decrease in AR at fixed $Re_{cr} - Re$ and κ increases Ω_{max}/G and decreases Ω_{min}/G; the range of torques 'sampled' by the freely rotating particle increases, leading to greater variation in angular acceleration and speed within a rotation period.

For periodic behaviour ($Re < Re_{cr}$), streamlines crossing at two off-surface stagnation points to the 'left' and 'right' of the cylinder divide the flow into five regions: a central streamline region around the rotating cylinder, two reversed flow regions, and two continuing flow regions. For an (x, y)-plane of the flow, the reversed flow regions to the left and right of the cylinder contribute a negative (clockwise) torque with magnitude $\mathscr{T}^-$; the continuing flow regions above and below the cylinder exert a positive (counterclockwise) torque with magnitude $\mathscr{T}^+$ (cf. figure 1) (DA00). The angular speed of the cylinder is maximum for a nearly vertical cylinder, and minimum for a nearly horizontal cylinder. The angular acceleration and torque on the cylinder should then be zero at these orientations.

Consider the dynamics of an elliptical cylinder of unit axial length (z-dimension) in a test section of width L when the cylinder is at its maximum angular speed Ω_{max} at a nearly vertical orientation (figure 15a). The magnitude of the torque on the cylinder due to the flow is the product of the viscous shear stress at the cylinder surface, the area over which this stress acts, and the moment arm (i.e. cylinder center to surface distance). If we assume that the velocity profiles near the cylinder surface are roughly linear, the continuing flow regions above and below the cylinder exert a positive torque $\mathscr{T}_v^+$ on the nearly vertical cylinder with magnitude

$$\mathscr{T}_v^+ \approx \mu \frac{\partial u}{\partial y} A^+ a \sim \mu \frac{0.5GL - \Omega_{max}a}{0.5L - a} ba = \mu ab \frac{G - \Omega_{max}\kappa}{1 - \kappa}, \qquad (4.1)$$
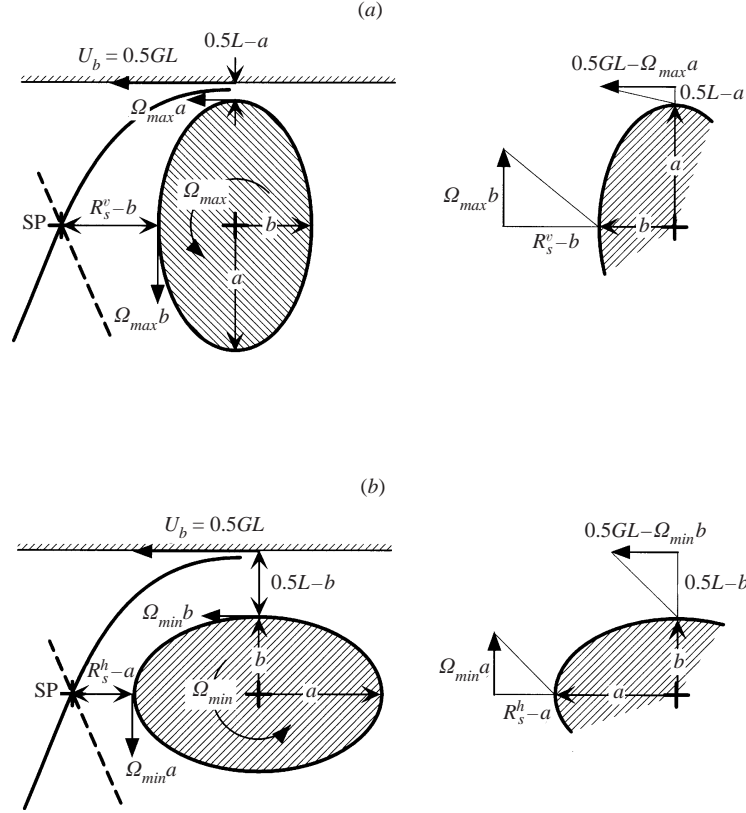
(*a*)

(*b*)

FIGURE 15. Definition sketch for scaling discussion in §4. (*a*) A vertically oriented elliptical cylinder in simple shear with an idealized linear velocity profile near the cylinder surface from both the Eulerian (left) and Lagrangian (right) viewpoints. (*b*) A similar sketch for a horizontal elliptical cylinder at minimum angular speed.

where μ is the fluid viscosity, u is the x velocity component and $\mathscr{T}_{\mathrm{v}}^{+}$ acts over cylinder surface area A^{+}. Similarly, the reversed flow regions exert a negative torque $\mathscr{T}_{\mathrm{v}}^{-}$ on the nearly vertical cylinder with magnitude

$$\mathscr{T}_{\mathrm{v}}^{-} \approx \mu \frac{\partial v}{\partial x} A^{-} b \sim \mu \frac{\Omega_{max} b}{R_s^v - b} ab, \tag{4.2}$$

where v is the y velocity component, $\mathscr{T}_{\mathrm{v}}^{-}$ acts over cylinder surface area A^{-}, and $R_s^v < a$ is the distance from the cylinder centre to the stagnation point at maximum angular speed (cf. figure 11). For zero torque, $\mathscr{T}_{\mathrm{v}}^{-} \sim \mathscr{T}_{\mathrm{v}}^{+}$, or

$$\frac{G - \Omega_{max}\kappa}{1 - \kappa} \sim \frac{\Omega_{max} b}{R_s^v - b}. \tag{4.3}$$

Solving for Ω_{max} gives

$$\frac{\Omega_{max}}{G} \sim \frac{R_s^v - a(AR)}{a(AR) + \kappa(R_s^v - 2a(AR))} < 1. \tag{4.4}$$

Next, consider the same elliptical cylinder when the cylinder is at its minimum angular speed Ω_{min} at a nearly horizontal orientation (figure 15*b*). Again modelling the velocity profiles near the cylinder surface as linear, the positive torque $\mathscr{T}_{\mathrm{h}}^{+}$ on the

nearly horizontal cylinder has magnitude

$$\mathscr{T}_{\mathrm{h}}^{+} \approx \mu \frac{\partial u}{\partial y} A^{+} b \sim \mu \frac{0.5GL - \Omega_{min} b}{0.5L - b} ab = \mu ab \frac{G - \Omega_{min}\kappa(AR)}{1 - \kappa(AR)}. \tag{4.5}$$

The negative torque $\mathscr{T}_{\mathrm{h}}^{-}$ on the nearly horizontal cylinder has magnitude

$$\mathscr{T}_{\mathrm{h}}^{-} \approx \mu \frac{\partial v}{\partial x} A^{-} a \sim \mu \frac{\Omega_{min} a}{R_s^h - a} ba, \tag{4.6}$$

where $R_s^h > a$ is the distance from the cylinder centre to the stagnation point at minimum angular speed (cf. figure 11). Balancing the two components and solving for Ω_{min} gives

$$\frac{\Omega_{min}}{G} \sim \frac{R_s^h - a}{a + \kappa(AR)(R_s^h - 2a)} < \frac{\Omega_{max}}{G}. \tag{4.7}$$

As expected, $\Omega_{min} = \Omega_{max}$ for $AR = 1.0$. As Re increases, the stagnation point approaches the cylinder surface, or $R_s^h \to a$, as $\Omega_{min}/G \to 0$, corresponding to stationary behaviour. Note that (4.4) and (4.7) depend upon Re; particle dynamics actually depend upon $Re_{cr} - Re$, where Re_{cr} varies with AR and κ.

If R_s^v and R_s^h vary weakly with AR, a decrease in AR for fixed Re, a and κ implies that Ω_{max}/G will increase for the moderate κ studied here ($\kappa \leqslant 0.5$), while Ω_{min}/G will decrease. The angular speed will therefore vary more over each rotation as AR decreases, in agreement with experimental results. Similarly, if R_s^v and R_s^h vary weakly with κ, an increase in κ for fixed Re, a and AR implies that both Ω_{max}/G and Ω_{min}/G will increase, again in agreement with experimental results.

As Re increases, the average distance from the cylinder centre to the stagnation point decreases for a given (AR, κ), implying that R_s^v and R_s^h also decrease as Re increases. For fixed a, AR, and κ, both Ω_{min}/G and Ω_{max}/G will therefore decrease as Re increases for $\kappa \leqslant 0.5$, again in agreement with experimental and numerical observations.

4.2. *Critical Reynolds number Re_{cr}*

To illustrate how aspect ratio affects critical Reynolds number, consider the two extreme cases: the circular cylinder at $AR = 1.0$, and the thin flat plate at $AR = 0$. The axisymmetry of the circular cylinder ensures a steady rotation rate and zero net torque upon the cylinder at any instant. We therefore expect $Re_{cr} \to \infty$ for $AR = 1$. For the thin plate, Jeffery's solution at zero Reynolds number predicts $T \to \infty$ at zero aspect ratio. At higher Re, a thin plate parallel to the flow would experience zero net torque because it has thin reversed flow regions and small moment arm with respect to the continuing flow regions, implying negligible $\mathscr{T}^-$ and $\mathscr{T}^+$, respectively. The critical Reynolds number is therefore zero for $AR = 0$. The experimental observations show that Re_{cr} varies continuously with AR between these two limits, increasing monotonically with AR from an undetermined value below 4 to an undetermined value above 25 as AR increases from 0.22 to 0.75, respectively.

Table 2 shows that both higher AR and increased flow confinement increase Re_{cr}. The cylinder exhibits stationary behaviour because the negative torque acting upon the cylinder as it approaches a horizontal orientation is great enough above a certain Re to decelerate the cylinder to rest. For a cylinder at a Reynolds number just below its critical value, an increase in the net torque $\mathscr{T} \equiv \mathscr{T}^+ - \mathscr{T}^-$ when the cylinder is near its equilibrium position will therefore lead to an increase in Re_{cr}.

We propose a simple scaling argument to explain the effects of both AR and

κ upon Re_{cr}. Consider again an elliptical cylinder of unit axial length at $Re_{cr} - Re = \varepsilon > 0$, where ε is small, rotating with positive angular speed Ω_h at a nearly horizontal orientation $\theta/\pi < 1$. The body will experience positive and negative torque components $\mathscr{T}_\mathrm{h}^+$ and $\mathscr{T}_\mathrm{h}^-$, respectively, given by (cf. (4.1) and (4.2))

$$\frac{\mathscr{T}_\mathrm{h}^+}{\mu ab} \sim \frac{G - \Omega_h \kappa(AR)}{1 - \kappa(AR)}, \qquad (4.8)$$

$$\frac{\mathscr{T}_\mathrm{h}^-}{\mu ab} \sim \frac{\Omega_h a}{R_s^h - a}. \qquad (4.9)$$

For a nearly horizontal cylinder just below the critical Reynolds number, Ω_h is close to the minimum angular velocity. DA00 showed that $\Omega_{min}/G \sim (Re_{cr} - Re)$ (cf. their equation (9) and figure 9). For this situation, $\Omega_{min}/G \sim \varepsilon$, and therefore $\Omega_h \ll G$. If R_s^h varies weakly with AR, (4.8) and (4.9) show that $\mathscr{T}_\mathrm{h}^+$ grows more rapidly than $\mathscr{T}_\mathrm{h}^-$ with AR for fixed Re, a and κ. The net torque $\mathscr{T}_\mathrm{h} \equiv \mathscr{T}_\mathrm{h}^+ - \mathscr{T}_\mathrm{h}^-$ will therefore increase as AR increases, implying that Re_{cr} increases with AR, in agreement with experimental results. Similarly, if R_s^h varies weakly with κ, (4.4) and (4.7) also show that $\mathscr{T}_\mathrm{h}^+$ grows more rapidly than $\mathscr{T}_\mathrm{h}^-$ with κ for fixed Re, a and AR. The net torque will therefore increase as κ increases, implying that Re_{cr} also increases as κ increases, again in agreement with experimental observations.

Figure 8 demonstrates that the $Re_{cr} - Re$ scaling already incorporates flow confinement effects on particle dynamics, in agreement with the hypothesis of DA00 that this scaling is independent of κ. Given that Poe & Acrivos (1975) saw no variation in rotation rate at $AR = 1$ for $0.18 \leqslant \kappa \leqslant 0.32$, and Zettner & Yoda (2001) observed significant variation in rotation rate at $\kappa = 0.39$ and 0.5, wall or flow confinement effects appear to be significant only above a certain level for circular cylinders. Similarly, flow confinement effects appear to be significant for elliptical cylinders only for $\kappa > 0.33$. Cylinders of $AR = 0.5$ at $\kappa = 0.33$ and $\kappa = 0.2$ (DA00) have virtually identical Re_{cr} values, while $AR = 0.5$ cylinders at $\kappa = 0.33$ and $\kappa = 0.42$ have significantly different Re_{cr} (7.3 for Cylinder F vs. 13.0 for Cylinder G).

Comparison of the results from two cylinders with the same AR based upon maximum outer dimensions but different local radii of curvature or cross-section shape – elliptical Cylinder D, vs. the nearly rectangular Cylinder C – shows that the cross-section shape affects the quantitative, but not the qualitative, behaviour of the body. Cylinder C and Cylinder D had significantly different Re_{cr} (7.3 vs. 4–5, respectively). Nevertheless, Cylinder C exhibited stationary behaviour for $Re > 7.3$, and the normalized rotation period of both cylinders was proportional to $(Re_{cr} - Re)^{-0.5}$ for $Re_{cr} - Re$ less than about 2. Moreover, the effects of decreasing $Re_{cr} - Re$ on angular orientation, speed and acceleration were qualitatively similar to those observed for elliptical cylinders. Given that this cylinder is markedly non-elliptical, these results, in conjunction with the scaling arguments of DA00, imply that particles with a broad variety of centrosymmetric cross-sections and particle-to-fluid density ratios will exhibit a transition to stationary behaviour above some critical Reynolds number. The results also support the conjecture of DA00 that if these centrosymmetric particles exhibit this transition, $GT \propto (Re_{cr} - Re)^{-0.5}$ and that this scaling is independent of particle shape.

An aspect ratio below unity, resulting in a time-varying torque on the cylinder at different angular orientations, appears to be the major prerequisite for transition to stationary behaviour above some critical Reynolds number. The scaling arguments in the previous subsections are independent of body shape, requiring only that the

principal axis along the maximum dimension of the body be nearly horizontal and vertical at maximum and minimum angular speeds, respectively. Given that Cylinder C fulfils these requirements (cf. table 3) and the experimentally observed effects of *Re* agree with the predictions of (4.4) and (4.7), we conjecture that the qualitative effects of *AR* and κ upon particle dynamics will be similar for both elliptical and non-elliptical cylinders of moderate aspect ratio.

5. Conclusions

These experiments have demonstrated that elliptical cylinders of *AR* from 0.33 to 0.52 cease rotating, coming to a complete rest at a nearly horizontal equilibrium orientation, above a critical Reynolds number Re_{cr} ranging from 4 to 13. To our knowledge, this is the first experimental confirmation of the results and conjectures of Ding & Aidun (2000). This behaviour is in marked contrast to that of cylinders at *AR* = 1, which continue to rotate at shear-based Reynolds numbers *Re* in excess of 70. In general, the particle dynamics scales with the difference between the critical and actual Reynolds numbers $Re_{cr} - Re$; rotation period scaled by shear rate is proportional to $(Re_{cr} - Re)^{-0.5}$ for small $Re_{cr} - Re$, in agreement with the scaling proposed by DA00. For stationary behaviour at $Re_{cr} - Re < 0$, the equilibrium orientation increases with decreasing $Re_{cr} - Re$ (i.e. as $Re \to Re_{cr}$), increasing *AR* and increasing κ. The data also strongly suggest that cylinders with aspect ratios beyond this range also exhibit this transition; only Reynolds numbers from 4 to 25 were accessible with the experimental facility used here, however.

In addition to verifying the lattice-Boltzmann simulations of DA00 for an *AR* = 0.5 elliptical cylinder at $\kappa = 0.2$, these experiments greatly extend the range of aspect ratio studied and address flow confinement issues. The results demonstrate that this surprising dynamical behaviour and scaling are valid for elliptical cylinders over a large range of aspect ratios, as conjectured by DA00. The dynamics of elliptical cylinders varies smoothly with aspect ratio between the extremes of a flat plate and a circular cylinder. Flow confinement appears to have minimal effects for $\kappa < 0.33$. Increases in aspect ratio and flow confinement (at values above 0.33) both increase critical Reynolds number.

Periodic behaviour of the elliptical cylinder at $Re_{cr} - Re > 0$ is characterized by rotation at a constant period but significant variation in angular speed. As $Re_{cr} - Re$ decreases, the maximum and minimum angular speeds of the cylinder both decrease. Moreover, the cylinder spends a greater fraction of its rotation period in a nearly horizontal orientation with low angular speed, reducing its angular speed averaged over a full rotation and increasing its period. In all cases, the period normalized by shear rate is proportional to $(Re_{cr} - Re)^{-0.5}$ for $Re_{cr} - Re$ below unity. The distance between each of the two stagnation points in this antisymmetric flow and the cylinder centre varies by almost half the ellipse semi-major axis over a full rotation. Each stagnation point moves in towards the centre as the angular speed increases to its maximum value, and moves out when the angular acceleration decreases to its minimum value. Maximum and minimum angular speeds scaled by shear rate increase and decrease, respectively, as *AR* decreases. Moderate changes in flow confinement appear to have little effect upon the particle dynamics at a given $Re_{cr} - Re$. Simple dynamics arguments are proposed to explain the observed effects upon critical Reynolds number and particle dynamics.

Interestingly, an *AR* = 0.33 non-elliptical cylinder also transitions from periodic to stationary behaviour, and its normalized period is also proportional to $(Re_{cr} - Re)^{-0.5}$

for small $Re_{cr} - Re$. Although deviation from elliptical cross-section also affects the value of the critical Reynolds number, elliptical and non-elliptical cylinders with the same moderate aspect ratio exhibit qualitatively similar dynamical behaviour, in agreement with the conjecture by Ding & Aidun (2000) that this scaling is 'universal'. We conjecture, based upon our simple arguments, that the qualitative effects of AR and κ upon particle dynamics will be independent of particle shape.

This work is, to our knowledge, the first experimental study of inertial effects upon the elliptical cylinder in simple shear flow. The marked effects of inertia in this fundamental unsteady two-dimensional bluff-body flow are clearly evident in the large differences between these results at non-zero Reynolds numbers and Jeffery's orbits. This study also represents a first step towards understanding how geometry and fluid inertia affect particle–fluid interactions in a two-dimensional dilute sheared suspension at non-zero Reynolds number. Although the results from this unsteady two-dimensional flow may not be directly applicable to three-dimensional suspensions (cf. Ingber & Mondy 1994, for example), understanding how geometric variations affect fluid–particle interactions is required to develop accurate physically based models for actual suspensions with multidisperse particles of varying shape.

These new experimental results strengthen the results and conjectures of DA00 on the dynamics of non-circular bodies in simple shear. Freely rotating centrosymmetric bodies with aspect ratio below unity sample different, or time-varying, torques in simple shear over one rotation period. As Reynolds number increases, the range of sampled torques increases, until the negative torque component is large enough to bring the cylinder to rest at a nearly horizontal orientation above some critical value. Nevertheless, several issues remain unresolved. Do all centrosymmetric bodies of arbitrary shape and density in simple shear with aspect ratio below unity and above zero transition to stationary behaviour? Or are there bodies with aspect ratios just below unity where the critical Reynolds number (if it exists) exceeds the Reynolds number limit for stable plane Couette flow? Since increased confinement appears to increase the critical Reynolds number, will highly confined bodies also exhibit this transition? These issues are relevant to both bluff-body flows and particle–fluid interactions in sheared suspensions.

REFERENCES

AIDUN, C. K., LU, Y. & DING, E. J. 1998 Direct analysis of particulate suspensions with inertia using the discrete Boltzmann equation. *J. Fluid Mech.* **373**, 287–311.

BARKLEY, D. & TUCKERMAN, L. S. 1999 Stability analysis of perturbed plane Couette flow. *Phys. Fluids* **11**, 1187–1195.

BECH, K. H., TILLMARK, N., ALFREDSSON, P. H. & ANDERSSON, H. I. 1995 An investigation of turbulent plane Couette flow at low Reynolds numbers. *J. Fluid Mech.* **286**, 291–325.

BOTTIN, S., DAUCHOT, O., DAVIAUD, F. & MANNEVILLE, P. 1998 Experimental evidence of streamwise

vortices as finite amplitude solutions in transitional plane Couette flow. *Phys. Fluids* **10**, 2597–2607.

DING, E. J. & AIDUN, C. K. 2000 The dynamics and scaling law for particles suspended in shear flow with inertia. *J. Fluid Mech.* **423**, 317–344 (referred to herein as DA00).

FENG, J. & JOSEPH, D. D. 1995 The unsteady motion of solid bodies in creeping flows. *J. Fluid Mech.* **303**, 83–102.

INGBER, M. S. & MONDAY, L. A. 1994 A numerical study of three-dimensional Jeffrey orbits in shear flow. *J. Rheol.* **38**, 1892–1843.

JEFFERY, G. B. 1922 The motion of ellipsoidal particles immersed in a viscous fluid. *Proc. R. Soc. Lond.* A **102**, 161–179.

KOSSACK, C. A. & ACRIVOS, A. 1974 Steady simple shear flow past a circular cylinder at moderate Reynolds numbers: a numerical solution. *J. Fluid Mech.* **66**, 353–376.

POE, G. G. & ACRIVOS, A. 1975 Closed-streamline flows past rotating single cylinders and spheres: inertia effects. *J. Fluid Mech.* **72**, 605–623.

RAFFEL, M., WILLERT, C. E. & KOMPENHANS, J. 1998 *Particle Image Velocimetry*. Springer.

TILLMARK, N. & ALFREDSSON, P. H. 1992 Experiments on transition in plane Couette flow. *J. Fluid Mech.* **235**, 89–102.

ZETTNER, C. M. & YODA, M. 2001 The circular cylinder in simple shear at moderate Reynolds numbers: an experimental study. *Exps. Fluids* **30**, 346–353.